JMEPEG (2019) 28:4693–4706
https://doi.org/10.1007/s11665-019-04228-3

1059-9495/$19.00

Effect of Microstructure Refinement on Hardness Homogeneity of Aluminum Alloy 1100 Processed by Accumulative Roll Bonding

Khaled J. Al-Fadhalah, Mohammed K. Alyazidi, and Mohammed Rafiq

(Submitted January 8, 2019; in revised form July 10, 2019; published online August 7, 2019)

This work examines the effect of grain refinement via accumulative roll bonding (ARB) on the homogeneity of microstructure and hardness through the thickness of commercially pure aluminum AA1100 sheets. The use of 7 cycles of ARB was shown to produce homogeneous ultrafine-grained microstructure, reducing the grain size to 0.46 and 1.03 µm in normal direction and rolling direction, respectively. Examination by electron backscattered diffraction indicates that continuous dynamic recrystallization was the main mechanism for the formation of submicron equiaxed grains bounded with high-angle grain boundaries (HAGBs). The fraction of HAGBs increased gradually reaching a maximum of 71.6% after 7 cycles. Through-thickness hardness measurements using Vickers and nanoindentation tests show an increase from 43.5 Hv (0.85 GPa) for as-received sample to 63 Hv (1.1 GPa) after 7 cycles. The heterogeneity in hardness through the thickness of the as-received material was shown to restrain the evolution of uniform hardness across the sheet thickness with increasing ARB cycles. Tensile tests showed that the tensile strength is increased to 250 MPa, which is about 2 times its initial value. Owing to the high stacking fault energy of AA1100, strong dynamic recovery occurred with increasing ARB strain which was balanced with the strain hardening property of the material. This resulted in plastic instability at small strains and thus early necking during the tensile test.

Keywords accumulative roll bonding (ARB), microhardness, microstructure, nanoindentation, pure aluminum

1. Introduction

Accumulative roll bonding (ARB) is a relatively new process that has been applied to induce severe plastic deformation (SPD) for the continuous production of metallic sheets with ultrafine-grained (UFG) structure, particularly in aluminum alloys. Originally developed by Saito et al. (Ref 1), ARB typically consists of multiple cycles of cutting, stacking and roll bonding of the sheet metals to 50% reduction in area. Depending on the nature of the material, significant structure refinement by ARB requires large plastic strain ($\varepsilon > 4$) that can be achieved after 5 cycles. In general, the large plastic deformation induced by ARB results in a reduction in grain sizes to submicron level, accompanied by an increase in grain boundary areas and in the fraction of high-angle grain boundaries (HAGBs). Also, it increases dislocation density due to strain hardening, which is commonly observed at the initial straining stages of SPD methods (Ref 2). In addition, applying large deformation during ARB causes a remarkable change in other crystal defects and introduces new surfaces and oxide films due to sheet stacking. This consequently affects the mechanical properties of the processed sheets, particularly increasing strength and hardness and lowering ductility. Consequently, brittleness, formation of edge cracks and delamination of the processed sheets might occur with increasing ARB cycles (Ref 3).

Several studies have focused on examining the development of microstructure and mechanical properties in ARB sheets of commercially pure aluminum (Ref 4-8). Pirgazi et al. (Ref 4) reported that the microstructure development by ARB in commercially pure aluminum is characterized by an increase in dislocation density and formation of subgrains or cell structures during the first 2 cycles. It was also found that the grain size was strongly reduced after 3 cycles and subgrains and dislocation cell structures started to form. Yet, Eizadjou et al. (Ref 5) indicated that few cycles of ARB in pure aluminum produced low dislocation density within the cell structure and the deformation was not homogeneous. In addition, Huang et al. (Ref 6) further examined the microstructure development in pure aluminum sheets processed by ARB and showed that multi-directional slips occurred at low ARB cycles, resulting in dislocations accumulation at subgrain boundaries and partial transformation of low-angle grain boundaries (LAGBs) into HAGBs. With increasing ARB cycles, breakage of the lamellar structure was observed that led to the development of homogenous UFG structure characterized by large fraction of HAGBs. Moreover, Kim et al. (Ref 7) examined the ultra-grain refinement by ARB in different aluminum alloys and showed that ARB resulted in an increase in strength and hardness with reducing grain size. In the case of AA1100, an increase in tensile strength was shown to occur after few ARB cycles to values 3 times greater than that found for the initial material.

Khaled J. Al-Fadhalah and **Mohammed K. Alyazidi**, Department of Mechanical Engineering, College of Engineering and Petroleum, Kuwait University, P.O. Box 5969, 13060 Safat, Kuwait; and **Mohammed Rafiq**, Nanotechnology Research Facility, College of Engineering and Petroleum, Kuwait University, P.O. Box 5969, 13060 Safat, Kuwait. Contact e-mail: khaled.alfadhalah@ku.edu.kw.

Yet, it has been observed that the ductility in AA1100 was reduced dramatically after few cycles due to limited strain hardening. The Hall–Petch behavior has also been demonstrated clearly by pure aluminum alloys processed by ARB. Another study by Scharnweber et al. (Ref 8) examined the use of ARB in AA1050 for 8 cycles and showed that the grain size was remarkably reduced to 0.5 μm. The strengthening via dislocation accumulation and grain size refinement resulted in an increase in the tensile strength following Hall–Petch behavior to about 2.5 the value of the initial material, while the ductility was initially reduced at the first 2 ARB cycles and later maintained at a moderate value of 12% at higher ARB cycles.

Different deformation modes can be imposed by ARB, which might lead to inhomogeneous development of microstructure and mechanical properties through the thickness of the processed sheets. Unlike conventional rolling, ARB requires no lubrication and thus large friction is produced between the surface of the sheet metals and the rolls. Consequently, the friction induces large redundant shear strain at the sheet subsurface regions, while plane strain compression mainly occurs at the center of the sheet. Thereby, a change in strain path is typically found through the thickness of the sheet metals processed by ARB. In addition, the large redundant shear strain at the sheet subsurface introduces non-uniform distribution of the deformation through the sheet thickness with increasing ARB cycles. This specifically occurs since the redundant shear strain becomes more distributed through the thickness with further sheet stacking. Consequently, the redundant shear strain can cause a great amount of heterogeneity in the microstructure and mechanical properties across the specimen thickness (Ref 9). Lee et al. (Ref 10) reported that inhomogeneous distribution of the Vickers microhardness occurred through the sheet thickness, with higher values near the surface at low ARB cycles. The high values of microhardness were justified by the strain hardening induced via redundant shear strain near the surface. With increasing ARB cycles, the hardening by the redundant shear strain near the surface further influenced the microhardness at the center of the ARB-processed specimens due to sheet stacking. It was also indicated that additional hardening occurred at the surface due to wire brushing. Despite that, the introduction of redundant shear strain due to friction has been found to majorly contribute to grain refinement and strengthening in sheets processed by ARB. Another work by Lee et al. (Ref 11) reported that the redundant shear strain is responsible for faster development of dislocation cells at small number of ARB cycles in AA1100. This was shown to be necessary for the production of UFG structure at ARB cycles higher than 5 cycles. It was also indicated that increasing ARB strain resulted in a larger fraction of HAGBs as compared to those formed in sample processed by conventional rolling. In addition, Huang et al. (Ref 6) showed that HAGBs in AA1100 samples processed by ARB reached misorientation saturation of 36° at a strain of 3.2, while it was not possible for HAGBs in conventionally rolled samples to reach misorientation saturation.

The above studies present strong evidence that redundant shear strain has a significant effect on the development of UFG microstructure and mechanical properties during ARB processing. Such strain can develop heterogeneity in the microstructure across the specimen thickness, particularly if the initial sheets were not homogeneous, which can be a detrimental factor on the mechanical properties and structural integrity of the bonded sheets. Besides that, the microstructure homogeneity and grain refinement are affected by the stacking fault energy (SFE) of the ARB material, which is strongly related to the ability of screw dislocations to cross-slip during deformation. Pure aluminum alloys possess high SFE, and thus it is possible for screw dislocation to cross-slip, providing faster rates of dynamic recovery to balance strain hardening during ARB deformation. This typically results in faster development of equilibrium UFG structure and ultimately saturation in strength and hardness after few ARB cycles.

The current study has examined the effect of ARB processing on the homogeneity of microstructure and mechanical properties of commercially pure aluminum AA1100. A special focus has been made on evaluating the effect of initial condition of the as-received aluminum sheets on the development of microstructure and hardness through sheet thickness during ARB. For a total of 7 cycles, ARB was applied at room temperature on the aluminum sheets using 50% reduction in area in each cycle. The development of UFG structure was examined using scanning electron microscopy (SEM) and electron backscattered diffraction (EBSD). Also, tensile properties of ARB samples were determined and through-thickness hardness was evaluated using Vickers microhardness and nanoindentation.

2. Materials and Methods

Commercially pure aluminum AA1100 sheets were received as rolled sheets in H14 temper condition, which typically involves work-hardening the sheets to half-hard without subsequent annealing. ARB strips were cut from the sheets having dimensions of 100 mm × 20 mm × 1 mm. The strips were then subjected to surface preparation. First, surface roughening of the strips was made using wire brushing. To ensure excellent bonding between the wire-brushed surfaces, the strips were placed in a bath of acetone in a sonication machine to remove contaminations, greases and oxides. The wire-brushed and acetone-cleaned sides were stacked together and fed into the rolling machine. The rolling machine was set to give a total reduction of 50% of the total thickness of the two stacked strips in each ARB cycle. The roll circumferential speed and diameter were 0.4 m/min and 65 mm, respectively. The stacked strips were rolled at ambient temperature without lubrication, and ARB was made up to 7 cycles. After rolling, the bonded strips were then cut into equal halves and the entire ARB steps were repeated until reaching the required number of ARB cycles.

To assess microstructure refinement by ARB, metallographic coupons were prepared for examination using SEM (model: JEOL 7001F-JSM). The coupons were cut from the cross section of ARB strips, i.e., a plane lying on the normal direction (ND) and rolling direction (RD), were ground and polished using standard metallography techniques. As a final polishing step, the coupons were processed using cross-section ion milling unit (model: JEOL SM-09010). Based on SEM imaging, grain size measurements were made along RD and ND and the average grain size was determined using the line intercept method. In addition, EBSD measurements were conducted to examine the development of different microstructure characteristics, including analysis of grain size, grain boundary character and grain boundary misorientation distri-

bution. As a final polishing step, the EBSD coupons were prepared using an electro-polishing unit (model: Struers-LectroPol5). The electro-polishing was made with an electrolyte containing 700 mL of ethanol, 100 mL of 2 butoxyethanol, 120 mL of water and 80 mL of perchloric acid, operated at 25°C with an applied potential of 24 V. The EBSD detector and post-processing software (model: Oxford-Aztec) were attached to the same SEM used in the current study. The EBSD maps were made at 2000× magnification with a step size range of 0.07-0.1 micron, using an operating voltage of 20 kV. The misorientation angle distribution statistics was analyzed, employing a critical misorientation angle of 15° to differentiate the low-angle boundaries (LAGBs) from the high-angle boundaries (HAGBs). The grain boundaries were presented in EBSD maps such that the LAGBs are depicted as gray lines and HAGBs as black lines. The average grain size was calculated according to ASTM: E112, using an average intercept method program available with the EBSD software. Also, kernel average misorientation (KAM) analysis was performed to evaluate the effect of ARB strains on accumulation of geometrically necessary dislocations (GNDs) responsible for these misorientations. KAM maps were constructed by computing the average misorientation between each measurement point and its neighbors, excluding grain boundaries with misorientation angle higher than 5°.

Tensile specimens of 1 mm thick were prepared from ARB strips and from the initial sheet metals. The tensile specimens were made according to ASME E8 standard with a gauge length of 25 mm (Fig. 1). Tensile tests were performed at room temperature using an electromechanical testing machine (Model: Instron 5581) with a crosshead speed of 0.75 mm/min. The ultimate tensile stress (UTS) of the sample was computed, and the ductility was determined by computing the percentage of elongation at fracture (%EL). In addition, SEM characterization of the fracture surfaces of the tensile specimens was performed in order to investigate the fracture behavior.

Through-thickness hardness measurements were first carried out using Vickers microhardness tester (model: Buehler Micromet). The microhardness indentations were made on metallographically prepared specimens cut from the ARB strips. The specimens were cold-mounted for surface sample preparation using the conventional procedure of grinding and polishing. The indentations were made at a load of 100 gf and dwell time of 15 s. Microhardness readings were taken through the sheet thickness, i.e., ND–RD plane, made 0.1 mm from the top surface of the sheet toward the bottom surface with an interval of 0.1 mm. For each interval, five measurement points were made, and the average of microhardness was calculated at each interval. In addition, through-thickness hardness at the nanoscale level of the ARB samples was evaluated using a nanoindentation tester (model: Hysitron-Ti700 UBI). Nanoindentation calibration was conducted following the Pharr–Oliver calibration method and using fused silica standard sample (Ref 12). Three-sided pyramid diamond Berkovich indenter was used to make the indentations, with a radius of curvature of 150 nm and an inclined angle of 142.3°. A load-controlled testing method was adapted with the load being applied gradually to a peak load of 8000 μN and held for 15 s, and then the load was gradually removed. For each sample, two lines of indentations were conducted through the sheet thickness. An average of 40 indentations was performed in each single array as schematically described in Fig. 2. The distances between two subsequent indentations were set to be 15 μm to avoid the effect from the plastic zone between the surrounding indentations. During gradual loading and unloading, the displacement of the indenter and the corresponding load was recorded for each indentation process. The hardness was determined from the load–displacement curves.

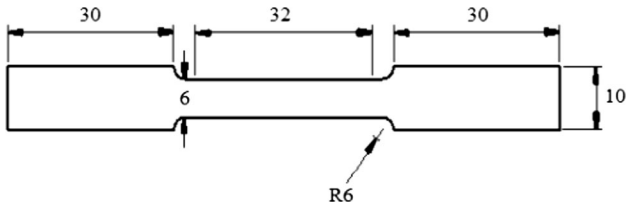

Fig. 1 Shape and dimensions of tensile test specimen. All dimensions are in mm

3. Results and Discussion

3.1 Microstructural Evolution

Figure 3 shows SEM micrographs for AA1100 samples in the as-received condition and after 1, 3, 5 and 7 cycles of ARB processing. It should be noted that curtaining effect (artifact lines in milled surfaces) is shown in the images due to the use of cross-section ion milling. The initial material, shown in Fig. 3(a), has a cellular microstructure that contains relatively large flat grains due to rolling deformation. The microstructure is also shown to contain a large amount of second-phase particles being uniformly distributed. Figure 3(b) provides the higher magnification of the initial sample that demonstrates the cellular formation of subgrains with size ranging from 1 to 10 μm. The ARB microstructure is typically identified by the spacing between lamellar boundaries and the spacing between transverse boundaries. During the ARB process, long lamellar boundaries formed parallel to RD, while short transverse boundaries were found to appear in the ND interconnecting the lamellar boundaries. Figure 3(c) presents the microstructure of ARB sample processed by 1 cycle, which clearly shows a remarkable reduction in grain size with most grains being elongated along the RD. At this stage, the equivalent ARB strain is about 0.8 that typically results in the formation of subgrains microstructures with LAGBs (Ref 4). At cycle 3, the grains are further refined and they are more elongated in the RD (Fig. 3d). Lamellar boundaries were also being formed with lamellar spacing less than 1 μm. Also, it can be seen that additional subgrain division occurred as illustrated by the formation of transverse boundaries. The use of 5 cycles resulted in further grain refinement with most grain being aligned with RD, as shown in Fig. 3(e). The lamellar boundaries are also seen to be strongly formed throughout the sample thickness. The lamellar spacing is generally less than 0.5 μm, while the spacing between transverse boundaries is about 1 μm. At cycle 7, a breakup of the lamellar structure is shown to occur and homogenous UFG structure is achieved as shown in Fig. 3(f). At this stage, the ARB strain is very high (∼ 5.6) that is expected to result in the formation of ultrafine grains with predominant HAGBs (Ref 4). Huang et al. (Ref 6) examined microstructure development in ARB of AA1100 and indicated that the spacing between the

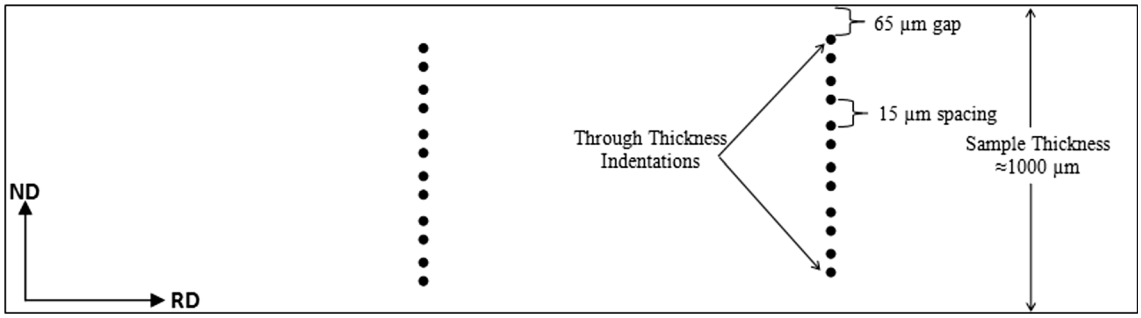

Fig. 2 Schematic illustration of nanoindentation test detailing through-thickness hardness measurements

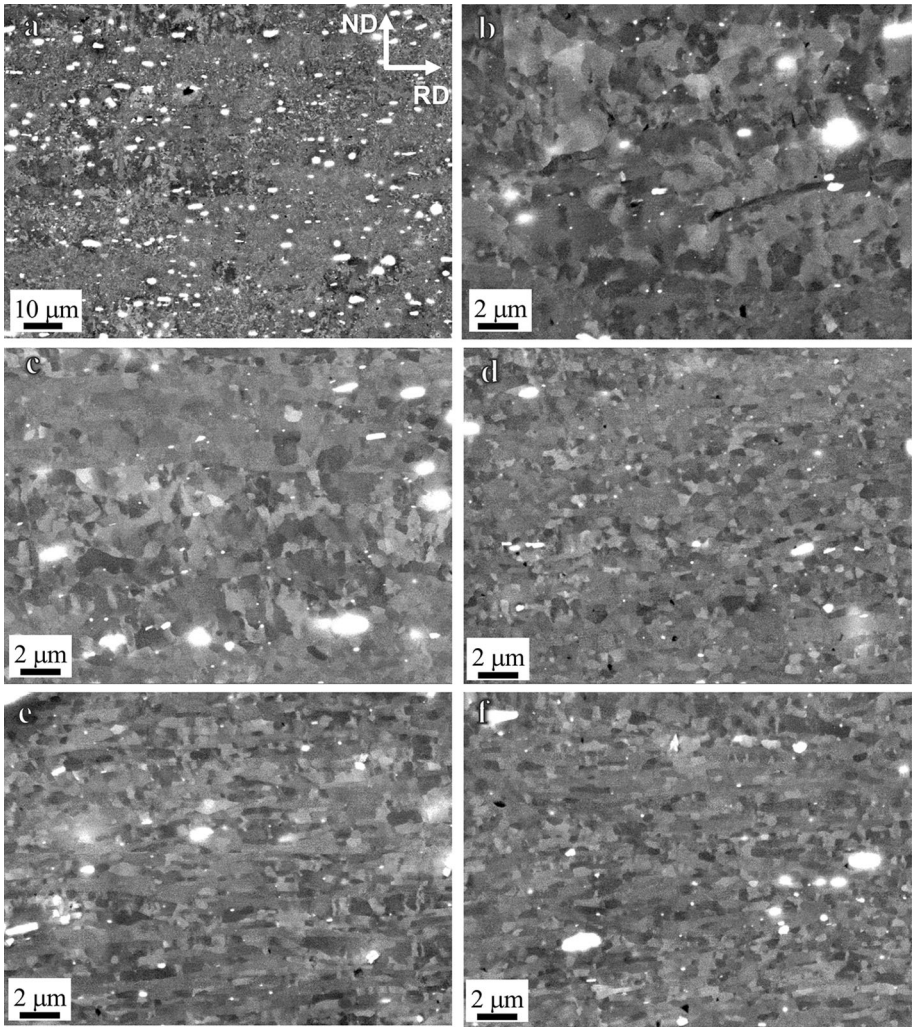

Fig. 3 SEM micrographs of AA1100 samples: (a, b) as received, (c) after 1 cycle, (d) 3 cycles, (e) 5 cycles and (f) 7 cycles

lamellar boundaries and that between the transverse boundaries decrease with increasing ARB strain. This was accompanied by an increase in the mean misorientation angle resulting in the formation of HAGBs. It was also shown that increasing ARB strain resulted in further formation of transverse boundaries due to dislocation glide between lamellar boundaries. On the other hand, lamellar boundaries did not additionally form with further ARB, but rather their misorientation angle continued to increase.

Figure 4 illustrates the grain refinement in the normal direction (ND) and rolling direction (RD) for AA1100 samples processed by ARB. The average grain size is initially large, being about 20 µm in ND and 31 µm in RD. Smaller grain size in ND was initially present since the initial material was received in rolling condition. Upon applying ARB, the grain size becomes much smaller in both directions, becoming about 0.74 µm in ND and 1.45 µm in RD. Most of the reduction in grain size occurred during the first 2 cycles. With further

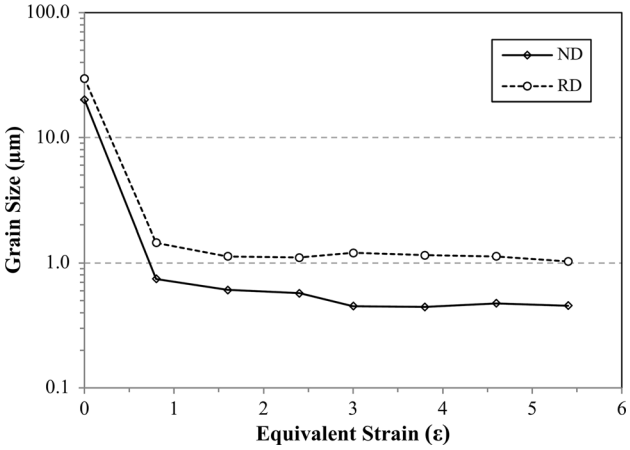

Fig. 4 Grain size measurements vs. ARB equivalent strain levels for AA1100 samples. Measurements in normal direction (ND) and rolling direction (RD)

increase in ARB cycles, the reduction continues to slowly occur reaching about 0.45 μm in ND and 1 μm in RD. Similar grain refinement was reported for AA1100 processed by ARB (Ref 4, 7).

Figure 5 shows the EBSD grain boundary construction maps for initial material and samples processed by 1, 3, 5 and 7 ARB cycles. The initial microstructure shown in Fig. 5(a) consists of large elongated grains along RD that contains subgrains and dislocation cells. The latter two substructures are typically formed in rolled metals and seen in EBSD by the formation of large fraction of LAGBs. Upon applying cycle 1, HAGBs are shown to form within the deformed structure (Fig. 5b). Yet, the LAGBs are still present within the initial deformed structure. At cycle 3, ultrafine grains of HAGBs develop within the microstructure (Fig. 5c). Yet, the fraction of LAGBs is still high. In cycle 5, UFG structure became prevailing and HAGBs are present by larger fraction (Fig. 5d). Most of the newly formed grains have size less 1 μm. At this stage, continuous dynamic recrystallization (CDRX) plays an important role in achieving submicron grain refinement in

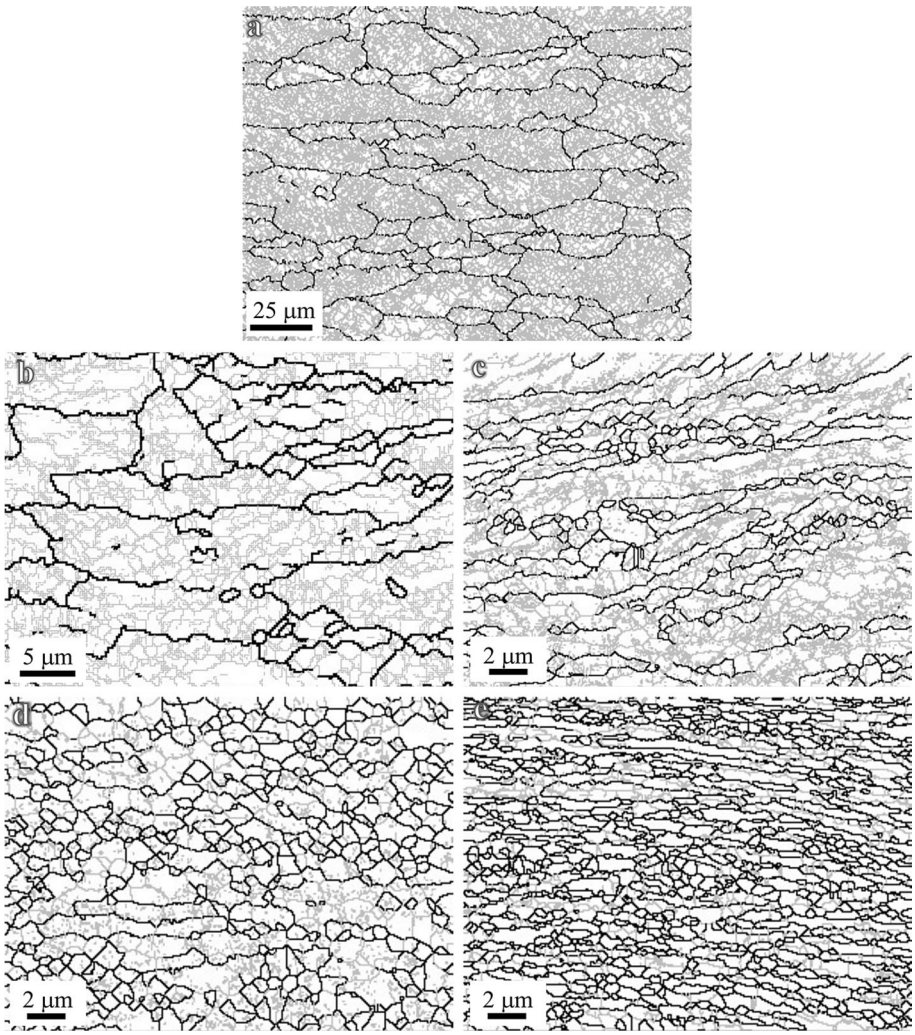

Fig. 5 EBSD maps of AA1100 samples processed by ARB: (a) as-received, (b) 1 cycle, (c) 3 cycles, (d) 5 cycles and (e) 7 cycles. Black lines represent HAGBs and gray lines represent LAGBs

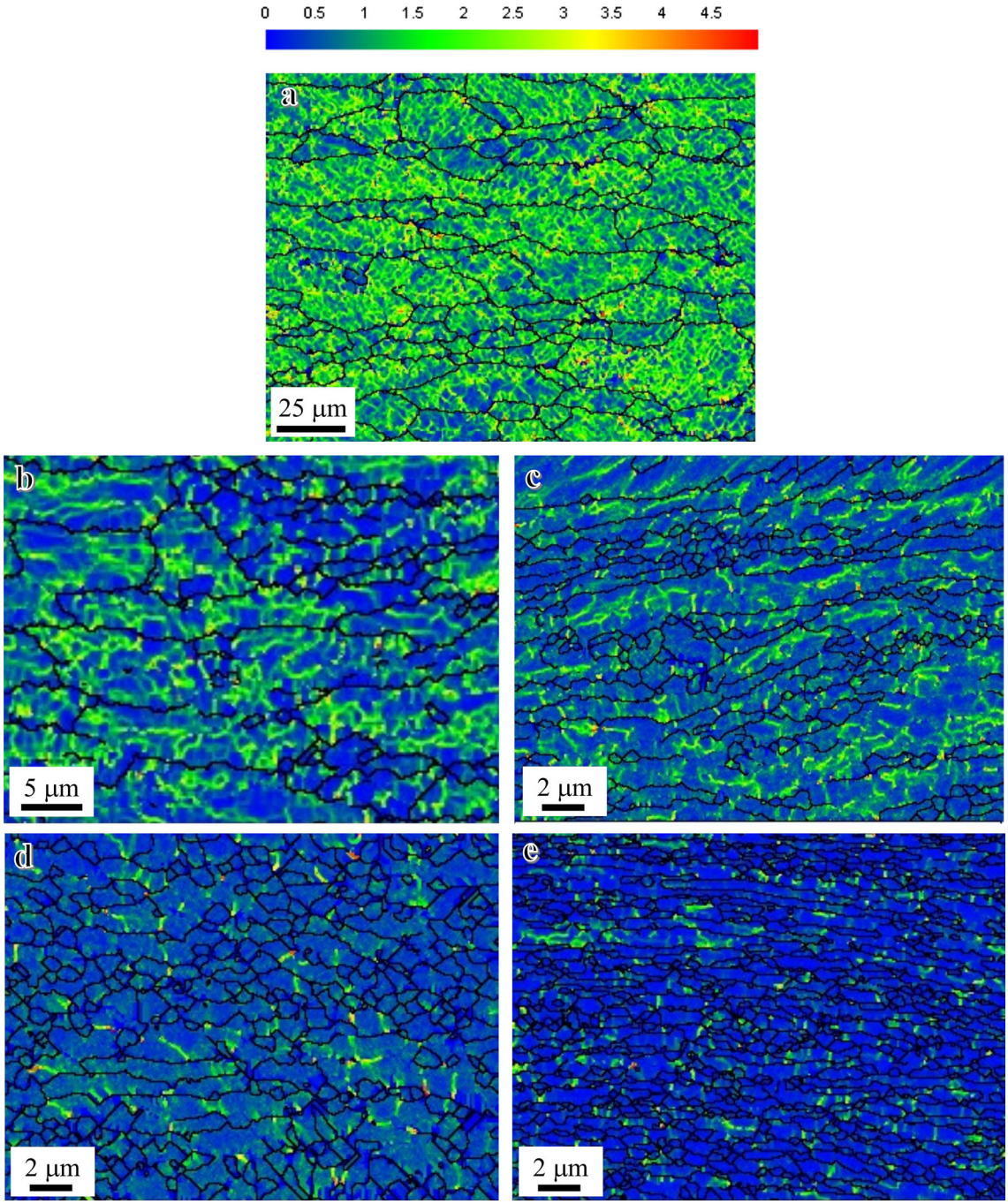

Fig. 6 Kernel average misorientation (KAM) maps of AA1100 samples processed by ARB: (a) as-received, (b) 1 cycle, (c) 3 cycles, (d) 5 cycles and (e) 7 cycles. Black lines represent HAGBs

aluminum alloys processed by ARB (Ref 13). Further ARB processing to cycle 7 resulted in an additional reduction in the average grain size and an increase in HAGBs, producing homogeneous UFG structure (Fig. 5e). It can also be noticed that the lamellar boundaries mostly have HAGBs. The spacing between these lamellar boundaries is generally less than 0.5 μm, extending 1-3 subgrains, while the spacing between transverse boundaries is reduced to about 1 μm. Moreover, Fig. 6 shows kernel average misorientation (KAM) maps highlighting development of local strain, associated with the formation of GNDs responsible for these misorientations, in the aluminum samples in as-received and ARB conditions. Brighter pixels indicate positions of abrupt orientation change in the microstructure. These mostly present LAGBs, and they are most likely interpreted as dislocation arrays. In general, there is a reduction in the KAM intensity with increasing ARB strain. This is consistent with further formation of HAGBs with increasing ARB cycles. Nevertheless, it should be noted that EBSD-based KAM maps only provide a qualitative analysis to the development of local strain rather than precise measurements of density of GNDs or total dislocation density.

Table 1 summarizes the EBSD measurements of the average grain/cell size and fraction of LAGBs for AA1100 samples. Initially, the microstructure contains large grains with high

Table 1 Statistics of EBSD data for AA1100 samples

No. of cycles	0	1	3	5	7
Equivalent ARB strain	0	0.8	2.4	4.0	5.6
Grain size—average, μm	11.0	2.4	1.08	0.88	0.72
Grain size—standard deviation, μm	9.3	1.4	0.64	0.47	0.43
LAGBs, %	88.6	83.5	73.3	33.8	28.4

fraction of LAGBs (88.6%). Cycle 1 resulted in a reduction in grain size to 2.4 μm, but the fraction of LAGBs is still high (83.5%). An additional decrease in grain size to 1.08 μm is shown to occur at cycle 3, accompanied with a reduction in the fraction of LAGBs. The development of UFG structure with HAGBs in cycle 5 resulted in further reduction in the grain size to 0.88 μm and lowering the fraction of LAGBs to a minimum of 33.8%. At this stage, additional accumulation of dislocations into the subgrain boundaries is expected to occur. This resulted in further transition of the grain boundaries from LAGBs to HAGBs. In cycle 7, the increase in ARB strain caused further reduction in grain size to an average of 0.72 μm, accompanied by a slight decrease in the fraction of LAGBs to 28.4%. At this high level of strain ($\sim$ 5.6), CDRX is still expected to become very active, leading to homogeneous UFG structure. Yet, local boundary migration and subgrain growth are possible to occur (Ref 14). This might significantly contribute to hinder any further grain refinement with increasing ARB strain.

Due to severe plastic deformation induced by ARB, the grain refinement of microstructure in materials with high SFE has been shown to be strongly related to CDRX (Ref 13). In such a case, homogeneous grain refinement at submicron level is achieved with predominant formation of high-angle boundaries. CDRX is generally characterized by grain subdivision, followed by dynamic recovery to form submicron grains, and then short-range grain boundary migration (Ref 15). This type of recrystallization is generally seen as a continuation of dynamic recovery. For the latter case, dislocation density is reduced by dislocation annihilation with other dislocations or grain boundaries or by dislocation rearrangement to form low-energy cells or subgrain structure. However, in CDRX, the subgrain structure continues to grow and extends its size to form stable low stored energy structure. For most metals plastically deforming at low strains, dislocation cells or subgrains of low-angle boundaries are formed. At moderate strains ($\varepsilon \approx 1$), the size of cells generally does not change very much. Yet, the mean boundary misorientation increases during deformation. As a result, many of LAGBs change into HAGBs with further increase in strain. Also, additional HAGBs form due to grain fragmentation. During large deformation and large accumulated strain, CDRX typically starts at HAGBs and continues until the subgrain boundaries are annihilated or increase their misorientations to form HAGBs.

A mechanism for the formation of UFG structure by CDRX in metals of SFE subjected to severe deformations has been modeled by Humphreys and Hatherly (Ref 14). The model requires that the initial material consists of lamellar microstructure of high-angle misorientation, which is aligned parallel to the RD, and intersecting boundaries that are mainly of low-angle misorientations. By applying large strain deformation, such as in ARB, it was proposed that localized boundary migration occurs, which results in the collapse of lamellar structure and formation of equiaxed grain structure. Nevertheless, Huang and Logé (Ref 16) reported that it is possible during CDRX to form HAGBs from microshear bands and/or kink bands rather than transferring LAGBs into HAGBs. In addition, Fig. 5(e) indicates that the lamellar thickness in the structure of sample processed by cycle 7 is very thin, i.e., thickness of very few subgrains. In such case, dynamic recrystallization can occur via the so-called geometric dynamic recrystallization (GDRX) (Ref 14). The latter mechanism is shown to occur when the deformed lamellar grains become highly elongated, having thickness below 1-2 subgrain size, and contain local serrations. With further thinning of the lamellar structure, the serrations are more likely to be pinched off and therefore it is possible to form equiaxed grains with HAGBs.

In the current study, CDRX is shown to occur in AA1100 samples with increasing ARB strain, as demonstrated by the formation of UFG structure with HAGBs. Early ARB studies reported that CRDX led to breakup of lamellar boundary due to the limited migration of HAGBs causing subgrain growth and formation of fine-equiaxed microstructure (Ref 17, 18). In addition, Kim et al. (Ref 7) indicated that second-phase particles and impurities provided additional boost to the grain refinement process during ARB processing of AA1100. The ultrafine grains possess HAGBs with their fraction reaching 64%. It was shown that the grains were more refined and equiaxed around the second-phase large particles and they were bent with the direction of these large particles. Far from the large particles, the grains were elongated in the RD. Another study by Chekhonin et al. (Ref 19) compared the effect of ARB on the microstructure development of commercially pure aluminum and that of high-purity aluminum. It was reported that ARB was sufficient to produce UFG structure in the commercial purity Al. For high-purity aluminum, relatively large grains (at the micron level) were formed due to the occurrence of partial CDRX. In addition, Jazaeri and Humphreys (Ref 20) showed that the presence of large second-phase particles (> 1 μm) in AA8001 increased the rate of formation of HAGBs by breaking up lamellar boundary structure. With further strain increase, additional formation of new HAGBs occurred in order to accommodate the large lattice rotations close to the particles. This emphasizes the important role of the second-phase particles on HAGBs' formation and grain refinement.

Moreover, the redundant shear strain induced by ARB has also been shown to affect the evolution of grain boundary misorientations and grain refinement in the current study. Up to 5 cycles, the grain refinement was not completely homogeneous (Fig. 3 and 5). With further increase in ARB cycles, the number of stacked layers in the ARB sheets increased and redundant shear strain was distributed more evenly throughout the sample thickness. This led to further homogeneity of the microstructure for high ARB cycles, but with no remarkable reduction in grain size. Lau (Ref 21) examined ARB of

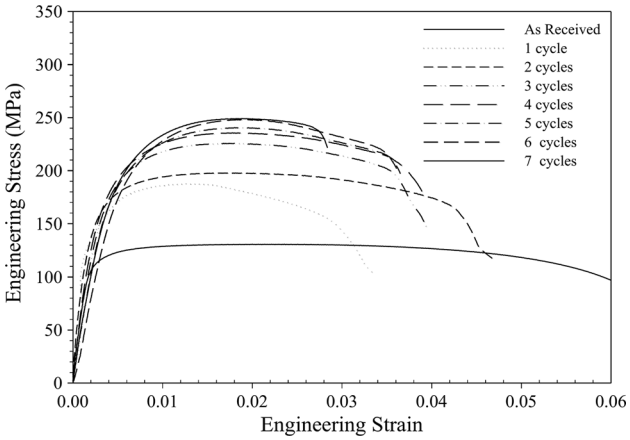

Fig. 7 Engineering stress–strain curves for AA1100 samples

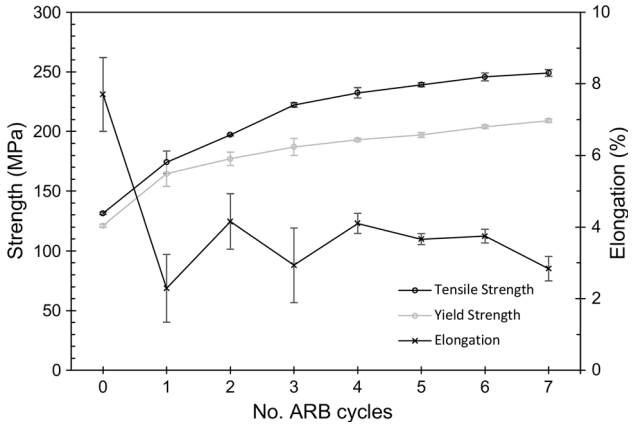

Fig. 8 Tensile properties for AA1100 samples

commercially pure aluminum and reported that the amount of strain during the first 3 cycles resulted in significant reduction in grain size. Increasing ARB cycles caused an increase in the misorientation of HAGBs, while it was difficult to form LAGBs since the grain refinement provided more obstruction to dislocations slips. The increase in misorientation of HAGBs continued to accommodate the ARB strain by cross-slip. The difference in the fraction of HAGBs and LAGBs between the subsurface and central region became less with increasing number of ARB cycles, resulting in homogenous UFG microstructure throughout the sample thickness. Another study by Li et al. (Ref 22) examined microstructure homogeneity by ARB. It was shown that redundant shear strain during ARB resulted in a variation in the grain size across the thickness of AA1100 samples, even after 6 cycles. The grain length was 582, 751 and 803 nm at the subsurface, quarter thickness and center regions, respectively. On the other hand, the grain thickness was to be the largest at the subsurface region (301 nm) and smallest at the center region (246 nm). Such variation is likely attributed to the large amount of shear strain and the heat generated in the subsurface region, which facilitated CDRX and eventually more formation of equiaxed ultrafine grains (Ref 6).

3.2 Tensile Properties

Figure 7 shows the plot of the engineering stress–strain curves of AA1100 samples subjected to ARB. For the as-received sample, the stress follows typical strain hardening behavior up to ultimate strength of approximately 130 MPa. The ductility is initially low (8%) since the as-received material was subjected to cold working prior to tensile testing. After the first cycle, the tensile strength increased to 180 MPa and strain to failure decreased to about 0.03. With increasing number of cycles, the tensile strength increased gradually to 250 MPa that is approximately 2 times the value of the as-received condition. The strain hardening behavior and tensile strength at the sixth and seventh cycles become almost similar. Previous studies on ARB of AA1100 reported similar tensile strengths, in the range of 250-310 MPa (Ref 4, 5, 7, 23, 24). Figure 8 shows the evolution of tensile properties with increasing number of ARB cycles. The elongation for AA1100 samples drops from 8% in as-received condition to about 2% after cycle 1. The ductility is slightly improved with increasing number of ARB cycles to 3-4%. On the other hand, increasing ARB cycles resulted in an increase in the yield strength from 122 to 208 MPa and the tensile strength from 131 to 249 MPa. Strong enhancement of strength is only seen to occur at low ARB cycles, while a limited increase in the strength occurred for high ARB cycles.

Fractography examination was made to identify the failure mechanisms and the bonding conditions in the ARB-processed aluminum samples. Necking was evident for all fractured tensile samples as visually inspected. Figure 9 illustrates the fracture surface of the tensile specimens, showing good bonding between the layers after fracture. Figure 9(a) presents the fracture surface of the as-received material, demonstrating a typical ductile fracture by having dimple formation in the center of the fracture surface and shear zones in the outside regions. The dimples (microvoids) are deep and hemispheroidal as shown in Fig. 9(b). The distinct dimple structure typically occurs due to the nucleation of microvoids, followed by their growth and coalescence (Ref 25). Figure 9(c) shows the fracture surface after 1 cycle of ARB, indicating signs of ductile fracture by having dimples in the center of each bonded layer and shear zones in the outside regions and also near the bonding line. Figure 9(d) shows that the formed dimples in the center region were relatively smaller and elongated, and not as deep as those in the as-received material. This suggests that the failure mode was shear ductile fracture and the amount of deformation and necking is less than that occurred in the initial material. With increasing ARB cycles, the fracture surfaces contained more bonding lines. Similar to the observations identified for 1-cycle sample, the fracture surface for samples processed by 3, 5 and 7 cycles shows the formation of dimple structure in the center region of each layer and shear zones near the bonding lines (Fig. 9e, g and i). It can also be noticed that the dimples became more hemispheroidal and deeper with increasing the number of ARB cycles (Fig. 9f, h and j). This indicates that the current aluminum samples became relatively more ductile at high ARB cycles.

In general, the evolution of tensile strength and ductility for AA1100 suggests that the samples were heavily deformed, resulting in strain hardening and loss in ductility. The capacity of strain hardening during tensile deformation can be evaluated by considering the difference between the tensile and yield strength (Fig. 8). For low ARB cycles, and prior to the development of UFG structure, the difference between the two strengths is small. With increasing ARB cycles, the difference between the two strengths continues to increase, indicating improvement in strain hardening capacity. However, the low

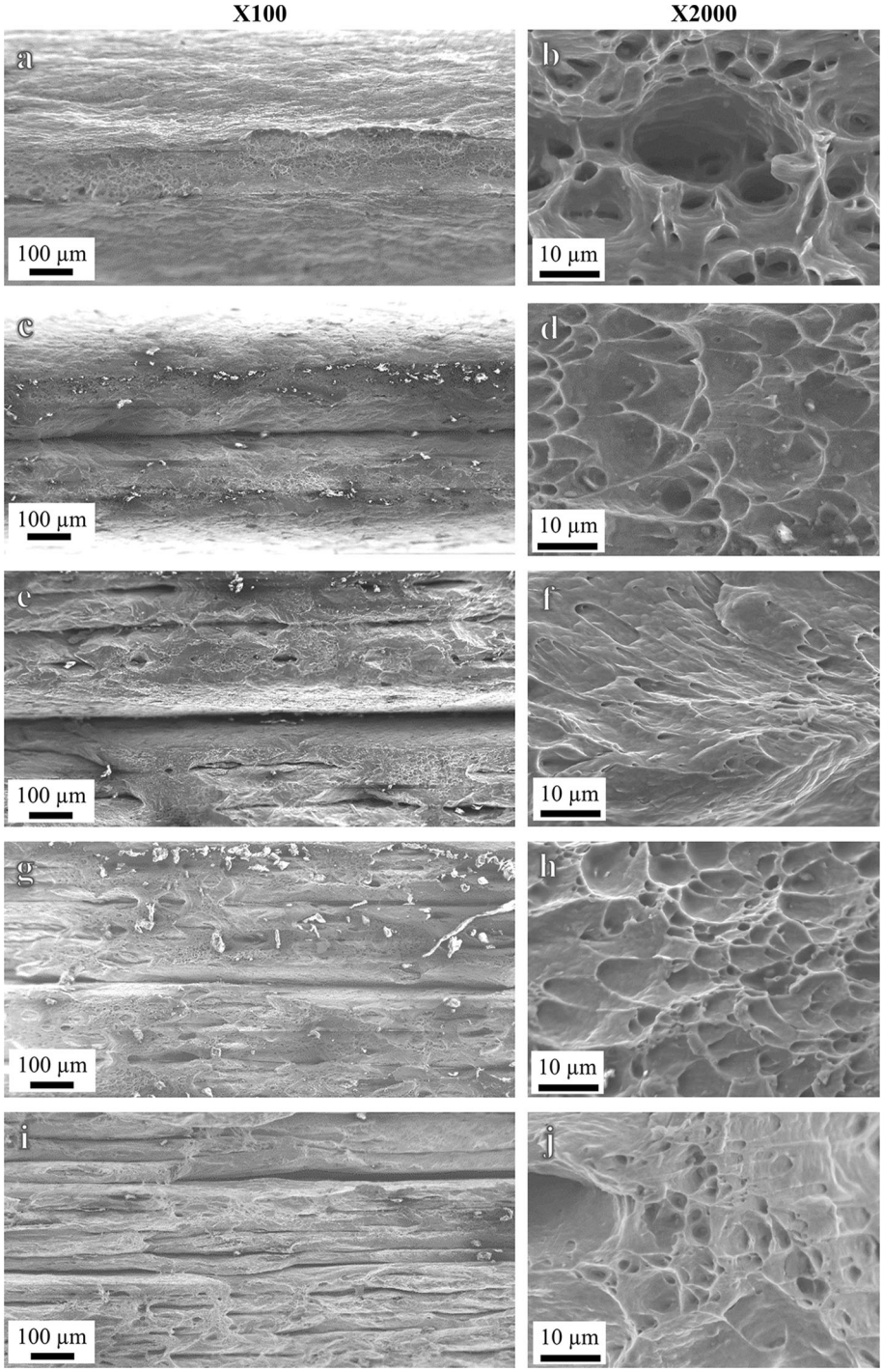

Fig. 9 Tensile fracture surfaces of: (a, b) as-received sample and ARB samples processed by (c, d) 1 cycle, (e, f) 3 cycles, (g, h) 5 cycles and (i, j) 7 cycles

ductility at high ARB cycles, compared to the initial material, suggests that the improvement in strain hardening is limited. At high ARB cycles, the dislocations' motion becomes more difficult with the increase in dislocation density due to severe plastic deformation and increase in the area of grain boundaries induced by grain refinement. The reduction in ductility by ARB has been shown to be related to plastic instability (Ref 26). Generally, plastic instability occurs when:

$$\sigma \geq \frac{d\sigma}{d\varepsilon} \qquad \text{(Eq 1)}$$

where σ is the flow stress and $\frac{d\sigma}{d\varepsilon}$ is the strain hardening rate. The grain refinement by ARB increases the flow stress, and simultaneously the strain hardening decreases. This makes the material prone to plastic instability, and thus necking and failure are expected to occur at smaller strains. Eizadjou et al.

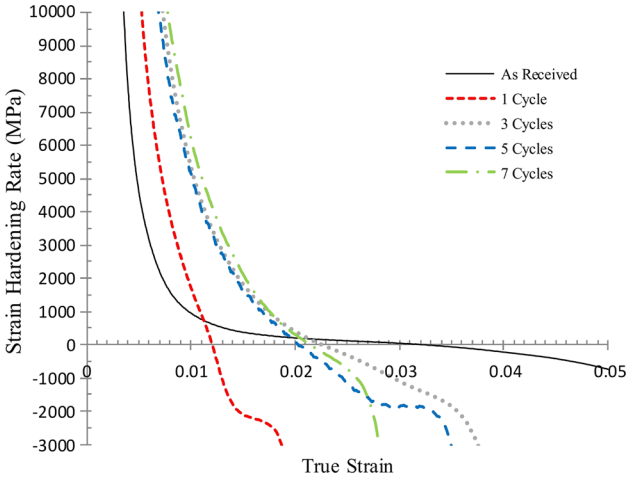

Fig. 10 Strain hardening rate vs. equivalent true strain for AA1100 samples

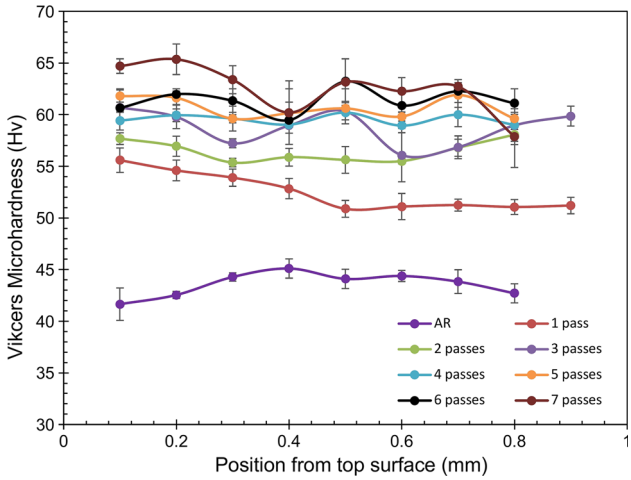

Fig. 11 Through-thickness Vickers microhardness for AA1100 samples

(Ref 5) indicated that the elongation in ARB AA1100 sheets was reduced from 39% in annealed condition to 3.3% after cycle 1. Surprisingly, the elongation was shown to increase to 4.6% after cycle 8. Also, Manna et al. (Ref 27) studied ECAP of AA1050 commercially pure aluminum and showed that elongation reduced after cycle 1 and later increased when processed by cycle 3. The increase in ductility was explained by the activation of different deformation mechanisms, besides strain hardening, such as sliding of grain boundaries and rotation of grains due to grain refinement.

The lack of strain hardening for ARB samples has been further examined by plotting strain hardening rate versus equivalent true strain as shown in Fig. 10. The sample in as-received condition displays positive strain hardening values to a relatively high strain ($\varepsilon \sim 0.03$), whereas the strain hardening rate of ARB samples drops rapidly below zero after smaller strains (0.01-0.02). Also, the strain hardening rate at small strains becomes higher with increasing number of cycles. Similar behavior has also been observed in previous studies (Ref 23, 28), which can be explained by the reduction in grain size with the increasing number of ARB cycles. The grain refinement has increased the number of grain boundaries encountering dislocations and thus resulted in further resistance to plastic deformation. The results also show that strain hardening becomes approximately similar at cycle 3 and higher. This suggests that the fast grain refinement in AA1100 samples has led to similar strain hardening after few ARB cycles. Unfavorably, plastic instability occurred at small strains for ARB samples. The instability is mostly attributed to the strong dynamic recovery in pure aluminum, causing faster loss in strain hardening rate and promoting necking. Therefore, limited increase in tensile strength occurred for samples processed by high ARB cycles.

3.3 Through-Thickness Hardness Evolution

Figure 11 shows Vickers microhardness measurements made through thickness for AA1100 samples in as-received condition and after processing by ARB. The Vickers microhardness tests were done in intervals of 0.1 mm through thickness of the ARB samples. The results show some variation in the through-thickness microhardness for AA1100 sample in as-received condition, having an average microhardness of 43.5 Hv. Upon applying cycle 1, the average microhardness increased to about 52.5 Hv. The increase in hardness was slightly higher on the sample surface. This is most likely due to the uneven distribution of pressure and/or friction induced from the rolls on bonded strips. Similar trend in hardness variation is seen in cycle 2, with an increase in hardness to an average of 56 Hv. In cycle 3, the average hardness is 60 Hv and there is more variation in hardness through the sample thickness. Further increase in ARB cycles resulted in limited strain hardening, producing small increase in the average hardness to a maximum of 63 Hv in cycle 7, with continuing variation in hardness across the sample thickness.

The microhardness profiles shown in Fig. 11 indicate an increasing inhomogeneity with increasing number of ARB cycles. This is most likely attributed to the redistribution of the redundant shear strain from surface regions toward the center of the sheets, and also to the increase in number of stacked strips with increasing ARB cycles (Ref 11). The through-thickness inhomogeneity might also happen during wire brushing used for preparing ARB samples, which can result in surface hardening (Ref 5). Such hardening results in uneven distribution of hardness through thickness, where additional hardening occurs at surface layers. Li et al. (Ref 22) examined the microstructural homogeneity of the evolution of hardness with ARB strain for different metallic materials, including commercially pure aluminum AA1100 in fully annealed condition. It was found that applying 6 cycles of ARB led to the formation of homogenous UFG structure, which in turn provided uniform distribution of microhardness through the thickness of ARB samples. Another study by Kwan et al. (Ref 23) examined the effect of annealing on microstructure and mechanical properties of ARB aluminum AA1100. The initial aluminum sheets were in fully annealed condition, and the microhardness was found to increase with increasing number of cycles up to 6 cycles and then decreased with increasing number of cycles. It was found that ARB processing by 6 cycles and higher resulted in the formation of stable microstructure. Unlike the findings in the above two studies, the use of AA1100 sheets in rolled condition has induced variation in microhardness in the initial material. This has been found to affect the homogeneity of hardness at high ARB cycles.

Further examination on the effect of hardness homogeneity by ARB processing was made using nanoindentation tests. The

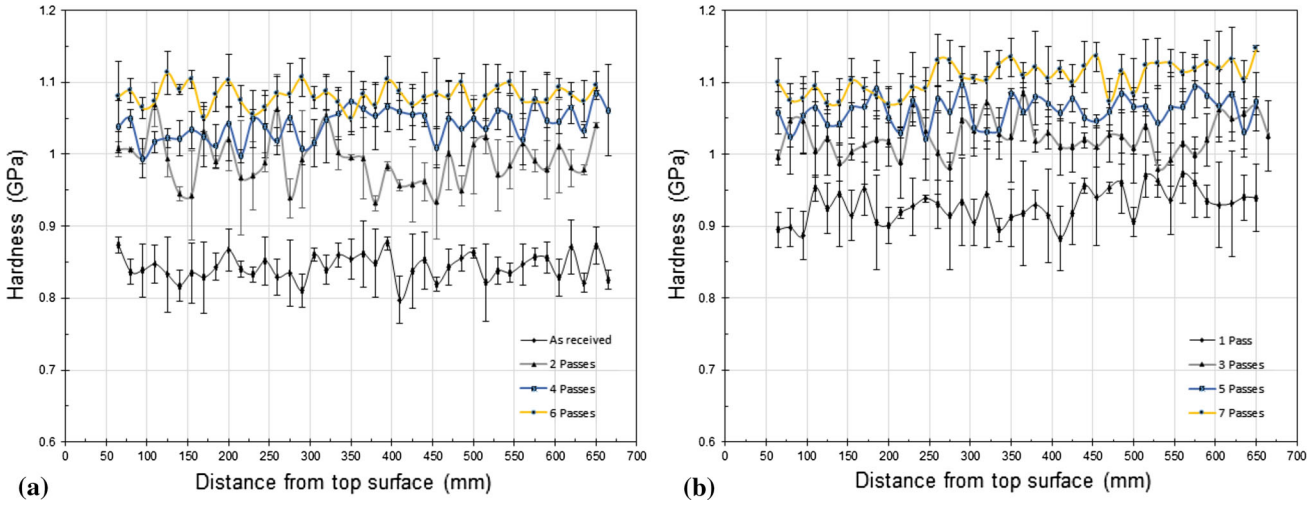

Fig. 12 Through-thickness nanoindentation hardness for AA1100 samples: (a) initial, 2, 4 and 6 cycles, (b) 1, 3, 5 and 7 cycles

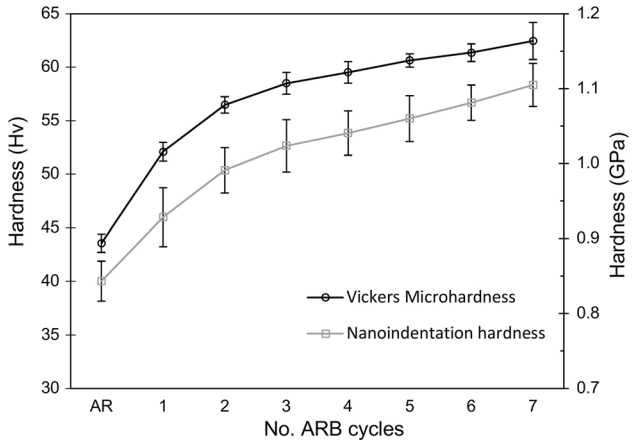

Fig. 13 Hardness evolution with ARB cycles for AA1100 samples

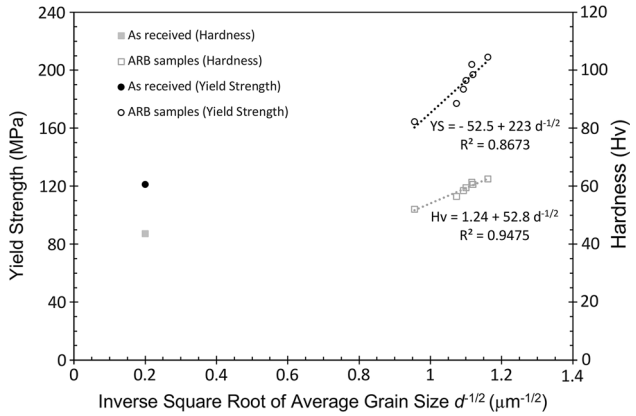

Fig. 14 Grain size dependency of AA1100 samples processed by ARB: yield strength and Vickers microhardness

results are plotted as shown in Fig. 12. In general, the average hardness increases remarkably in the first 2 cycles from an average of 0.85 GPa in the as-received condition to about 1.0 GPa at cycle 2. At higher cycles, the average hardness slowly increases to a maximum of 1.1 GPa. Similar to the microhardness results, the through-thickness measurements of hardness using nanoindentation show that hardness heterogeneity initially existed in the as-received condition. The heterogeneity increased in the first few ARB cycles due to the uneven distribution of the redundant shear strain, particularly with the accumulation of additional rolled strips. Nevertheless, the hardness becomes less scattered with increasing number of ARB cycles. This suggests that the UFG structure becomes more uniform with increasing ARB strains.

Figure 13 compares the average hardness obtained by nanoindentation test with measurements of Vickers microhardness as a function of ARB cycles, accompanied by their standard deviation. The results generally show similar hardness evolution using the two indentation methods, demonstrating a large increase in hardness during the first 2 ARB cycles and later limited increase in hardness with increasing ARB cycles. This suggests that the hardness approximately saturates to its maximum value due to the balance between dislocation generation (via strain hardening) and dislocation annihilation (via dynamic recovery). In addition, the standard deviation of the hardness generally decreases with increasing ARB cycles, except for cycle 7. Yet, it should be noted that the values of standard deviation for nanoindentation are relatively large, compared to Vickers microhardness measurements, due to the dependency of hardness on contact depth at the nanoscale level, demonstrating the so-called indentation size effect (ISE) (Ref 29). In general, the results presented in Fig. 13 suggest that the initial heterogeneity in the hardness continued to exist in the ARB samples, but it decreased with increasing ARB cycles. The fast dynamic recovery in AA1100 after few ARB cycles led to uniformity of the UFG structure and thus less variation in through-thickness hardness at high ARB strains.

3.4 Grain Refinement Strengthening

Figure 14 presents the yield strength and hardness change with the grain size for the aluminum samples in initial condition

and after ARB processing. The results generally show an increase in yield strength (YS) and hardness (Hv) with reducing grain size (d). Such dependency holds the Hall–Petch (HP) relation, which requires the yield strength and hardness to vary as the inverse square root of grain size (Ref 30, 31). The HP relation for yield strength is generally described by:

$$YS = \sigma_0 + k_{HP} d^{-1/2} \quad \text{(Eq 2)}$$

where σ_0 and k_{HP} are material constants. Typically, σ_0 represents the frictional stress resisting the motion of gliding dislocations, while k_{HP} is the HP slope defined as the resistance of the grain boundary against slip transfer. For the examined ARB aluminum samples in the current study, the two constants were determined as $\sigma_0 = -52.5$ MPa and $k_{HP} = 0.223$ MPa.m$^{1/2}$. High values of k_{HP} and negative σ_0 were also reported by Kamikawa et al. (Ref 32), who examined strengthening mechanisms in high-purity aluminum severely deformed and annealed. High k_{HP} values were interpreted by the developed structure that consists of relatively coarse equiaxed grains (2-5 μm) with a mixture of LAGBs and HAGBs. It was suggested that additional strengthening mechanisms are required to operate, including dislocation strengthening from LAGBs and individual dislocations between the boundaries.

In addition, Wyrzykowski and Grabski (Ref 33) made an extensive study on the HP relation in aluminum alloys and indicated that there is a considerable scatter of experimental results of HP constants reported in the literature. The scattering was proposed to be related to: different texture development in the polycrystalline aluminum samples that affects the orientation factor M and thus the value of frictional stress σ_0, and variation in grain boundary diffusivity (higher diffusivity lowers the value of HP slope k_{HP}). It was also reported that for the case of UFG structure in pure aluminum, with grain size in the range of 0.4-1.4 μm, the HP relation was characterized by $\sigma_0 = -30$ MPa and $k_{HP} = 0.093$ MPa.m$^{1/2}$. The scattering of HP constants for aluminum alloys was also reported by Thangaraju et al. (Ref 34), who indicated that there is a substantial scatter in the values of k_{HP} from 0.06 to 0.28 MPa.m$^{1/2}$, having the highest for cryo-milled AA 5083 alloy and the lowest for pure metal Al in hot extrusion condition.

Moreover, Hansen (Ref 35) extensively examined the HP relation for yield stress (flow stress) of undeformed and deformed polycrystalline metals. For samples deformed to large strains, many of LAGBs were found to evolve into HAGBs. In such a case, the contribution of both types of boundaries was considered into the HP relation by the replacing the grain size with the average boundary spacing. This was particularly applied for heavily cold-rolled metallic sheets where a lamellar structure is typically formed having different spacing between the lamellar boundaries and the interconnecting boundaries. It was also indicated that the HP slope for deformed samples is much higher than obtained for samples in annealed conditions, when comparing similar grain size range. In aluminum, a heavily cold-rolled sample has $k_{HP} = 0.14$ MPa.m$^{1/2}$, while recrystallized aluminum has $k_{HP} = 0.04$ MPa.m$^{1/2}$. It was also reported that high k_{HP} and negative σ_0 occurred in cold-rolled Ni samples, suggesting that another mechanism can be operative at nanoscale levels, where there might be no enough space for the pileups or for the operation of Frank–Read sources. In addition, Ma et al. (Ref 36) indicated that there is a deviation in the HP relationship in UFG materials fabricated by SPD processes, including materials processed by ARB. It was suggested that such deviation is mainly attributed to the fact that the effective grain size used in the HP relation is larger than the measured value since it is possible for mobile lattice dislocations to pass easily through the non-equilibrium grain boundaries formed in the materials processed by SPD. More recently, Huang et al. (Ref 37) examined the HP behavior in UFG structure of Al-0.3%Cu processed by heavy cold-rolling. It was found that when the grain size is reduced to sub-micrometer scale, k_{HP} is raised and it became no longer independent of the grain size. It was suggested that additional strengthening mechanisms, other than boundary strengthening, can be operative including lattice strengthening, solid solution strengthening, dislocation strengthening and particle strengthening.

On the basis of the above-mentioned studies, it is clear that the ultra-grain refinement cannot be the sole mechanism responsible for strengthening the current pure aluminum processed by ARB. Tsuji et al. (Ref 26) suggested that other mechanisms can contribute to the increase in the strength of materials processed by ARB, such as strain hardening and texture strengthening, and the increase in HAGBs fraction induced by high ARB strains. During the first few cycles of ARB, the dislocation density typically increases and subgrains and/or cell structures form (Ref 38). At this stage, strain hardening is the major strengthening mechanisms. In particular, the increase in forest dislocations and grain boundaries area hinders dislocation mobility and thus requires additional stress to overcome the stress fields. For pure aluminum, the SFE is high (200 erg/cm^2) that leads to high rate of dislocation climb and cross-slip and thus fast recovery rate during deformation (Ref 39). With further increase in ARB strain, the rate of strain hardening and dynamic recovery is expected to reach dynamic equilibrium, which results in constant dislocation density and development of UFG structure. In such case, grain refinement becomes more effective strengthening mechanism than strain hardening (Ref 5). Most of the increase in the strength is shown for the current material to occur at the first few cycles, before the saturation of dislocation density. Consequently, the contributing factors of strength enhancement are thought to be mainly attributed to strain hardening at small ARB strains, and later to strengthening by grain refinement at high ARB strains. Nevertheless, details of the strengthening mechanisms in the current material should be further examined, particularly the evolution of dislocation density. This is also important in the case of heavily rolled material of UFG structure, where both dislocation strengthening from LAGBs and grain size strengthening from HAGBs can significantly contribute to the strength (Ref 35).

4. Conclusions

ARB has been applied to 7 cycles on commercially pure aluminum AA1100 to examine the microstructure development and through-thickness homogeneity of the hardness. The following conclusions can be drawn:

(1) Microstructure examination of the ARB samples indicates a change in the grain size from 10 to 20 μm in the initial structure into 0.6-0.7 μm after 7 cycles. Strong

grain refinement occurred during the first 3 cycles, after which the reduction in grain size became limited. Yet, the development of homogeneous UFG structure was also seen after 5 cycles, accompanied by an increase in HAGBs. The high SFE of the pure aluminum led to faster dynamic recovery during ARB deformation and thus promoted CDRX required for the ultra-grain refinement.

(2) Through-thickness hardness measurements using Vickers microhardness and nanoindentation indicate an increase in hardness with increasing ARB cycles. It was found that the heterogeneity of the initial aluminum sheets in rolled condition has prevented the development of uniform hardness distribution. This was also affected by the redundant shear strain occurring at the subsurface regions and the stacking nature of ARB sheets that resulted in inhomogeneous distribution of strain through the sample thickness.

(3) Tensile strength gradually increased with increasing ARB cycles, reaching a maximum of 250 MPa after 7 cycles. Yet, a reduction in the ductility to about 2%EL occurred, which was strongly attributed to the large drop in strain hardening rate, leading to plastic instability at small tensile strains. The increase in yield strength and hardness with grain refinement was demonstrated by Hall–Petch effect.

Acknowledgments

The authors would like to acknowledge the support provided by Kuwait University General Facility (Grant No. GE 01/07) for sample preparation and SEM and EBSD measurements.

References

1. Y. Saito, H. Utsunomiya, N. Tsuji, and T. Sakai, Novel Ultra-high Straining Process for Bulk Materials Development of the Accumulative Roll-Bonding (ARB) Process, *Acta Mater.*, 1999, **47**(2), p 579–583
2. J. Chang, G. Kim, and I. Moon, X-ray Diffraction Analysis of Pure Aluminum in the Cyclic Equal Channel Angular Pressing, *Scr. Mater.*, 2001, **44**, p 331–336
3. N. Tsuji, Y. Saito, S. Less, and Y. Minamino, ARB (Accumulative Roll-Bonding) and Other New Techniques to Produce Bulk Ultrafine Grained Materials, *Adv. Eng. Mater.*, 2003, **5**, p 338–344
4. H. Pirgazi, A. Akbarzadeha, R. Petrovb, and L. Kestensc, Microstructure Evolution and Mechanical Properties of AA1100 Aluminum Sheet Processed by Accumulative Roll Bonding, *Mater. Sci. Eng. A*, 2008, **497**, p 132–138
5. M. Eizadjou, H.D. Manesh, and K. Janghorban, Microstructure and Mechanical Properties of Ultra-fine Grains (UFGs) Aluminum Strips Produced by ARB Process, *J. Alloy. Compd.*, 2009, **474**, p 406–415
6. X. Huang, N. Tsuji, N. Hansen, and Y. Minamino, Microstructural Evolution During Accumulative Roll-Bonding of Commercial Purity Aluminum, *Mater. Sci. Eng. A*, 2003, **340**, p 265–271
7. H.-W. Kim, S.-B. Kang, N. Tsuji, and Y. Minamino, Elongation Increase in Ultra-fine Grained Al–Fe–Si Alloy Sheets, *Acta Mater.*, 2005, **53**, p 1737–1749
8. J. Scharnweber, W. Skrotzki, C.-G. Oertel, H.-G. Brokmeier, H.W. Höppel, I. Topic, and J. Jaschinski, Texture, Microstructure and Mechanical Properties of Ultrafine Grained Aluminum Produced by Accumulative Roll Bonding, *Adv. Eng. Mater.*, 2010, **12**, p 989–994
9. K. Wu, H. Chang, E. Maawad, W.M. Gan, H.G. Brokmeier, and M.Y. Zheng, Microstructure and Mechanical Properties of the Mg/Al Laminated Composite Fabricated by Accumulative Roll Bonding (ARB), *Mater. Sci. Eng. A*, 2010, **527**, p 3073–3078
10. S.H. Lee, Y. Saito, T. Sakai, and H. Utsunomiya, Microstructures and Mechanical Properties of 6061 Aluminum Alloy Processed by Accumulative Roll-Bonding, *Mater. Sci. Eng. A*, 2002, **325**, p 228–235
11. S.H. Lee, Y. Saito, N. Tsuji, H. Utsunomiya, and T. Sakai, Role of Shear Strain in Ultragrain Refinement by Accumulative Roll-Bonding (ARB) Process, *Scr. Mater.*, 2002, **46**, p 281–285
12. W.C. Oliver and G.M. Pharr, An Improved Technique for Determining Hardness and Elastic Modulus Using Load and Displacement Sensing Indentation Experiments, *J. Mater. Res.*, 1992, **7**, p 1564–1583
13. N. Tsuji, R. Ueji, Y. Ito, Y. Saito, In-situ Recrystallization of Ultra-fine Grains in Highly Strained Metallic Materials, *Proceedings of the 21st RISØ International Symposium on Materials Science*, Denmark, 2000, pp 607–616
14. F.J. Humphreys and M. Hatherly, *Recrystallization and Related Annealing Phenomena*, 2nd ed., Elsevier, Kidlington, 2004
15. F.J. Humphreys, P.B. Prangnell, and R. Priestner, Fine-Grained Alloys by Thermomechanical Processing, *Curr. Opin. Solid State Mater. Sci.*, 2001, **5**, p 15–21
16. K. Huang and R.E. Logé, A Review of Dynamic Recrystallization Phenomena in Metallic Materials, *Mater. Des.*, 2016, **111**, p 548–574
17. M. Shaarbaf and M.R. Toroghinejad, Nano-grained Copper Strip Produced by Accumulative Roll Bonding Process, *Mater. Sci. Eng. A*, 2008, **473**, p 28–33
18. S. Pasebani and M.R. Toroghinejad, Nano-grained 70/30 Brass Strip Produced by Accumulative Roll-Bonding (ARB) Process, *Mater. Sci. Eng. A*, 2010, **527**, p 491–497
19. P. Chekhonin, B. Beausir, J. Scharnweber, C. Oertel, T. Hausol, H.W. Hoppel, and W. Skrotzki, Confined Recrystallization of High-Purity Aluminum During Accumulative Roll Bonding of Aluminum Laminates, *Acta Mater.*, 2012, **60**, p 4661–4671
20. H. Jazaeri, F.J. Humphreys, The Recrystallization of a Highly Deformed Al–Fe–Mn Alloy, *Proceedings of first International Conference on Recrystallization and Grain Growth*. Aachen, Germany, 2001, pp 27–31
21. K.D. Lau, "Development of Microstructure and Texture in Accumulative Roll Bonded Commercial Purity Aluminium," Master's thesis, University of New South Wales, Australia, 2011
22. B. Li, N. Tsuji, and N. Kamikawa, Microstructure Homogeneity in Various Metallic Materials Heavily Deformed by Accumulative Roll-Bonding, *Mater. Sci. Eng. A*, 2006, **423**, p 331–342
23. C. Kwan, Z. Wang, and S.B. Kang, Mechanical Behavior and Microstructural Evolution Upon Annealing of the Accumulative Roll-Bonding (ARB) Processed Al Alloy 1100, *Mater. Sci. Eng. A*, 2008, **480**, p 148–159
24. M. Raei, M.R. Toroghinejad, and R. Jamaati, Nano/Ultrafine Structured AA1100 by ARB Process, *Mater. Manuf. Process.*, 2011, **26**, p 1352–1356
25. R.W. Hertzberg, *Deformation and Fracture Mechanics of Engineering Materials*, 3rd ed., Wiley, Singapore, 1989, p 253–257
26. N. Tsuji, Y. Ito, Y. Saito, and Y. Minamino, Strength and Ductility of Ultrafine Grained Aluminum and Iron Produced by ARB and Annealing, *Scr. Mater.*, 2002, **47**, p 893–899
27. R. Manna, N.K. Mukhopadhyay, and G.V.S. Sastry, Effect of Equal Channel Angular Pressing on Microstructure and Mechanical Properties of Commercial Purity Aluminum, *Metall. Mater. Trans. A*, 2008, **39**, p 1525–1534
28. L. Su, C. Lu, A.K. Tieu, G. Deng, and X. Sun, Ultrafine Grained AA1050/AA6061 Composite Produced by Accumulative Roll Bonding, *Mater. Sci. Eng. A*, 2013, **559**, p 345–351
29. W.D. Nix and H. Gao, Indentation Size Effects in Crystalline Materials: A Law for Strain Gradient Plasticity, *J. Mech. Phys. Solids*, 1998, **46**, p 411–425
30. E.O. Hall, The Deformation and Ageing of Mild Steel: III, Discussion of Results, *Proc. Phys. Soc.*, 1951, **64**, p 747–753
31. N.J. Petch, The Cleavage Strength of Polycrystals, *J. Iron Steel Inst.*, 1953, **173**, p 25–28
32. N. Kamikawa, X. Huang, N. Tsuji, and N. Hansen, Strengthening Mechanisms in Nanostructured High-Purity Aluminium Deformed to High Strain and Annealed, *Acta Mater.*, 2009, **57**, p 4198–4208
33. J.W. Wyrzykowski and M.W. Grabski, The Hall–Petch Relation in Aluminium and Its Dependence on the Grain Boundary Structure, *Philos. Mag. A*, 1986, **53**, p 505–520
34. S. Thangaraju, M. Heilmaier, B.S. Murty, and S.S. Vadlamani, On the Estimation of True Hall–Petch Constants and Their Role on the

Superposition Law Exponent in Al Alloys, *Adv. Eng. Mater.*, 2010, https://doi.org/10.1002/adem.201200114
35. N. Hansen, Hall–Petch Relation and Boundary Strengthening, *Scr. Mater.*, 2004, **51**, p 801–806
36. K. Ma, H. Wen, T. Hu, T.D. Topping, D. Isheim, D.N. Seidman, E.J. Lavernia, and J.M. Schoenung, Mechanical Behavior and Strengthening Mechanisms in Ultrafine Grain Precipitation-Strengthened Aluminum Alloy, *Acta Mater.*, 2014, **62**, p 141–155
37. T. Huang, L. Shuai, A. Wakeel, G. Wu, N. Hansen, and X. Huang, Strengthening Mechanisms and Hall–Petch Stress of Ultrafine Grained Al–0.3%Cu, *Acta Mater.*, 2018, **156**, p 369–378
38. Y. Murata, I. Nakaya, and M. Morinaga, Assessment of Strain Energy by Measuring Dislocation Density in Copper and Aluminium Prepared by ECAP and ARB, *Mater. Trans.*, 2008, **49**, p 20–23
39. A. Rezaee-Bazzaz, S. Ahmadian, and H. Reihani, Modeling of Microstructure and Mechanical Behavior of Ultrafine Grained Aluminum Produced by Accumulative Roll Bonding, *Mater. Des.*, 2011, **32**, p 4580–4585